# Tectonic Regime as a Control Factor for Crustal Fault Zone (CFZ) Geothermal Reservoir in an Amagmatic System

**H. Duwiquet[1,2,3], F. Magri[4,5], S. Lopez[1], T. Guillon[1], L. Arbaret[2], M. Bellanger[3], and L. Guillou-Frottier[1,2]**

[1]BRGM, Georesources Division, Av. C. Guillemin, BP 36009, F-45060 Orléans Cedex 2, France.

[2]ISTO, UMR 7327, University of Orléans, CNRS, BRGM, 1A Rue de la Férollerie, 45071, Orléans, France.

[3]TLS-Géothermics, 91 Chemin de Gabardie, 31200 Toulouse, France.

[4]Department of Environmental Informatics (ENVINF), Helmholtz Centre for Environmental Research (UFZ), Leipzig, Germany.

[5]Freie Universität Berlin, Department of Hydrogeology, Berlin, Germany.

Corresponding author: Hugo Duwiquet (hugo.duwiquet@gmail.com)

**Key Points:**

- As a potential geothermal reservoir, crustal fault zones remain largely unexplored and therefore unexploited.
- Different tectonic regimes influence fluid flow.
- The poroelasticity driven force explains why strike-slip CFZs could be considered as interesting targets for geothermal power system.

## Abstract

The Crustal Fault Zones provides an interesting geological target for high temperature geothermal energy source in naturally deep-fractured basement areas. Field and laboratory studies have already shown the ability of these systems to let fluid flow down to Brittle-Ductile-Transition. However, several key questions about exploration still exist, in particular the fundamental effect of tectonic regimes on fluid flow in fractured basement domains. Based on poroelasticity assumption, we considered an idealized 3D geometry and realistic physical properties. We examined a model with no tectonic regime (benchmark experiment) and a model with different tectonic regimes applied. Compared to the benchmark experiment, the results suggest that different tectonic regimes cause pressure changes in the fault/basement system. The tectonic-induced pressure changes affect fluid patterns, onset of convection as well as the spatial extent of thermal plumes and the intensity of the temperature anomalies.


## 1 Introduction

Usually, the formation of a geothermal resource requires the presence of fluid, a drain and a heat source. Permeable faults are natural drains for fluids circulation and have a rising scientific and economic interest for mineral (e.g. lithium) and geothermal resources (Saevarsdottir et al., 2014; Liang et al., 2018, Guillou-Frottier et al., 2020). Crustal Fault Zones (CFZ) are geological structures that localize deformation (Ben-Zion and Rovelli, 2014) and modify the petrophysical properties of the crust above Brittle-Ductile-Transition (BDT). CFZ are defined by faults network and interconnected fractures which extension vary from of a few meters to several kilometers. Field and laboratory observations show a succession of damage zones and fault cores corresponding to the multiple fault core conceptual model of Faulkner et al. (2003). Within the interconnected fracture networks of the Pontgibaud Crustal Fault Zone, the presence of pores at different scales (from 2.5 µm to 2 mm) facilitates fluid flow (Duwiquet et al., 2021). CFZ are widely present around the globe. They are found in Chile - Atacame Fault System - (Mitchell and Faulkner, 2009), Germany - Badenweiler-Lenzkirch Sutur – (Brockamp et al., 2015), or Finland - Pasmajärvi Fault Zone - (Ojala et al., 2019). These geological structures can be located in different geological settings (magmatic or amagmatic) and different tectonic stress regimes. This paper investigates the role of the tectonic regime on geothermal reservoirs within and around CFZ, in amagmatic systems.

Although CFZ provide potential renewable and economic geothermal resources, they remain largely unexplored and undeveloped. Thus, full understanding of the processes that impact fluid flow in CFZ is a prerequisite for successful exploration. Recent work has shown that pressure and temperature conditions can induce fluid flow near the BDT (Violay et al., 2017; Watanabe et al., 2017; 2021). Fluid-filled fractures have been observed down to mid-crustal depths, as shown by the deep boreholes of the Kola Peninsula (Kozlovsky, 1984), and the German KTB continental deep drill hole (Grawinkel and Stöckhert, 1997; Ito and Zoback 2000). Additionally, Famin et al. (2004) suggested that massive infiltration of surface-derived fluids occurred in a detachment shear zone of Tinos Island (Greece), down to a depth of 10-15 km. Similarly, Siebenaller et al. (2013) demonstrated that meteoric fluid infiltration occurs down to the BDT (around a depth of 8 km) in the Naxos detachment fault (Greece).

Convection around geothermal wells is mandatory to reach production power that leverage the high drilling cost of deep borehole. When the permeability is too low, the strategies developed

by the Enhanced Geothermal System (EGS) technique increase the permeability by different injection phases, among which hydraulic stimulations aim at causing hydro-shearing and/or hydro-fracturing. These methods have allowed the development of many geothermal power plants, such as Soultz-sous-Forêts, Upper Rhine Graben, France (Genter et al., 2010). However, the seismicity induced by these injection phases have jeopardized several geothermal projects (Deichmann and Giardini, 2009, Evans et al., 2005). Between 2020 and 2021 in Alsace (France) a series of induced earthquakes of magnitude M=3, M=3.6, M=3.9 caused the definitive shutdown of the geothermal project and raised doubts in the population. Since 2020, the United Downs Deep Geothermal Project (UDDGP) is attempting to target a naturally fractured reservoir in the heat-producing Cornish granite (Ledingham et al., 2019; Paulillo et al., 2020). Drilling through the sub-vertical, strike-slip Porthtowan fault zone has induced an earthquake of magnitude M = 1.5 (www.inducedearthquakes.org), too small to be felt by local population. These naturally fractured zones can then be areas where the risk of induced seismicity is limited.

The complex nature of the interactions between Thermal (T), Hydraulical (H), Mechanical (M) and Chemical (C) couplings affect the behavior of the geothermal reservoir under natural conditions. Numerical modeling has been used since 1945 to understand the controlling factors of fluid circulations (Horton and Rogers, 1945; Katto & Masuoka, 1967; Horne, 1979; Forster & Smith, 1989; López & Smith, 1995; O'Sullivan et al., 2001; Magri et al., 2016; Guillou-Frottier et al., 2020). Tectonic deformation has been considered as driving forces that influence fluid flow in different geological contexts (Ord and Oliver, 1997b; Cox, 1999; Rowland and Sibson, 2004). Bethke (1985) shows that compressive environments can lead to increased fluid pressure and favor upward movement. Sibson (1987) links overpressure and upward movement to fault valve activity. In extensional environments, the generated under-pressure appears to cause downward fluid migration (McLellan et al., 2004). Nevertheless, none of them have looked at the effect of tectonic regime on fluid flow, and the consequences on the temperature anomalies in CFZ. Cui et al. (2012) used simplified 2D models with a fault zone to show that with degrees of shortening exceeding 1% the fluid flows whose driving force was buoyancy forces is then different. In 3D models, Eldursi et al. (2020) suggest that during tectonically active periods, the decrease in pore pressure can reorient fluid flow in fractured zones.

Fluid flow velocities, and thus efficiency of heat transport by convection through the crust, are directly controlled by the permeability of the rocks. Permeability is a dynamic and variable parameter that can change during different geological processes (Gleeson and Ingebritsen, 2016). The relationship between permeability and porosity is widely debated. Although adapted to porous media, the Kozeny-Carman relationship does not seem appropriate for fractured media (Lamur et al., 2017; Parisio et al., 2019).

In CFZs, fluid circulation driven by buoyancy forces occurs through upward and downward movement localizing positive temperature anomalies at shallow depths (Duwiquet et al., 2019; Guillou-Frottier et al., 2020). These 2D and 3D TH numerical modeling studies have shown that vertical or subvertical deep deformation zones could concentrate the most important temperature anomalies at the lowest depths. However, these results do not consider poroelastic effects on fluid flow. Poroelastic models describe the interaction between fluids and deformation in the porous medium. The fluids in a reservoir are affected by stresses whether on their pressure (undrained conditions in low-permeable media with, e.g., increase in pressure under compressive stress state), or on their circulation (drained conditions in permeable media with, e.g., convection

from more to less compressed regions). Our previous study, which includes poroelasticity, suggested that vertical deformation zones oriented at 30° and 70° to a maximum horizontal stress could correspond to potential targets for high temperature geothermal energy (Duwiquet et al., 2021). Thus, the stress orientation has an effect on the fluid flow. In anisotropic boundary conditions, these effects are expected to be strongly accentuated. Indeed, they introduce shearing conditions favorable to dilation. These aspects could be treated in mechanical terms, which would allow the calculation of slip tendency, defined by the ratio of shear stress and effective normal stress (Morris et al., 1996).

Here, we investigate, the role of tectonic regimes on the formation of an amagmatic geothermal reservoir (i.e. the only heat is the natural geothermal flux) within a CFZ and without any other heat source than the natural geothermal flux (amagmatic system). We propose a faulted 3D THM numerical model with a simplified geometry. The physical properties are realistic and the hydraulic permeability is adapted to the fractured environment. In order to understand the role of tectonic regimes, we first considered a benchmark experiment that neglects tectonic stress. This result is compared to several numerical experiments where tectonic stresses are implemented.

The effect of the poroelasticity-driven force on fluid flow will differ from one tectonic regime to another and impact the formation of a HT geothermal reservoir in fractured environment. The observed differences can be mainly explained by different lateral fluid pressure variation. This paper highlights the importance of mechanical effects in geothermal processes. The tectonic induced pressure changes affect fluid patterns, onset of convection, the spatial extent of thermal plumes and the intensity of the temperature anomalies.

## 2 Materials and Methods

Comsol Multiphysics$^{TM}$ software is based on the Finite Element Method (FEM) and can, among other various physical processes, model fluid flow, heat transfer and elastic deformation of materials in a 3D geometry. Comsol Multiphysics$^{TM}$ is a well-known tool offering a complete access to the solution of partial differential equations. Benchmark tests have already been performed with previous numerical codes (OpenGeoSys, Comsol Multiphysics$^{TM}$ v3.5a, see Guillou-Frottier et al., 2020 and Appendix 1).

We consider an idealized and synthetic model that represents a typical vertical fault zone of 400 m thickness, in the middle of a 5.5 km side cubic volume of homogeneous basement rock. The fault zone, which corresponds to a multiple fault core, is treated like continuous porous medium. At very high fracture density, this assumption seems to be convenient (Zareidarmiyan et al., 2021). The mesh is defined by 15,785 tetrahedra, with mesh sizes of 500 m for low permeability zones and mesh sizes of 170 m for high permeability zones. Preliminary convergence tests have shown that a finer mesh size gives the same results. The transient simulations are run up to 990 kyrs. The vertical faces of the basement are thermally insulated and fluid circulation is blocked. On the upper horizontal face, a temperature of 20°C and a pressure of 105 Pa are imposed (Fig 1).

The initial thermal regime corresponds to a geothermal gradient of 30°C/km. At the base of the model a heat flux of 100 $mW.m^{-2}$ is imposed. This heat flux can represent the sum of the mantle heat flow and the heat emitted by the decay of radioactive elements in the crust. The fluid is assumed to be pure water, and the fluid density depends on the pressure and temperature conditions (as detailed in Duwiquet et al., 2021). The details of the equations between Darcy's

law, Fourier's law and Hooke's law can also be found in Duwiquet et al. (2021). All thermal, hydraulic and mechanical parameters are detailed in Table 1:

**Table 1 : Set of physical parameters used in numerical modelling. *Fault zone permeability is variables and adapted to fractured media (see Eq 3).**

| Category | Symbols | Fault zone | Basement | Unit |
|---|---|---|---|---|
| Porosity | $\Phi$ | 0.1 | 0.05 | - |
| Permeability | k | Variable* | $10^{-16}$ | $m^2$ |
| Thermal conductivity | $\lambda_s$ | 3 | 2 | W/(m.K) |
| Heat capacity | $Cp_s$ | 800 | 800 | J/(kg.K) |
| Bulk density | $\rho_s$ | 2700 | 2700 | $kg/m^3$ |
| Young's modulus | E | 5 | 60 | GPa |
| Poisson's ratio | v | 0.30 | 0.25 | - |
| Biot-Willis coefficient | $\alpha_B$ | 0.8 | 0.8 | - |

The Young's moduli imposed in the numerical models are suitable for fault zone and basement (Cappa and Rutqvist, 2011). In the basement, the Poisson's ratio is 0.25, a value generally accepted in the literature. However, in the fault zone we impose a value of 0.30. This value can be explained by two aspects, the first one is that the samples on which the Poisson coefficients are measured are much smaller than the block considered. This change of scale tends to increase the value of the Poisson coefficient (Heap et al., 2020). In addition, weathering and fracturing processes present in fault zones tend to increase the value of the Poisson's ratio (Heap et al., 2020). The physical properties of the fluids are identical to the study by Duwiquet et al. (2021).

In order to investigate the influence of tectonic regimes on fluid flow, we will compare a model with no tectonic stresses applied (which we will call the "benchmark experiment") with models where different tectonic regimes are considered. For these models, we have free boundary condition at the top, and clamping at the bottom (displacement blocked in all three directions). For the four vertical sides of the model, we use mechanical boundary conditions corresponding to the evolution of the stress with depth for different tectonic regimes. For this, we refer to an Andersonian assumption -where the principal stresses are expressed with vertical Sv, maximum horizontal SHmax and minimum horizontal Shmin components- which is regularly used in geomechanical studies of reservoirs (Anderson, 1905; Zoback et al., 2003):

- Compressional (reverse/thrust faulting), $S_{Hmax} \geq S_{hmin} \geq S_V$

- Extensional (normal faulting) with, $S_V \geq S_{Hmax} \geq S_{hmin}$

- Strike-slip, with, $S_{Hmax} \geq S_V \geq S_{hmin}$

In order to understand the possible effects of stress intensity, stress-depth profiles were collected on two natural systems, one in the French Massif Central, and one near the San Andreas Fault. Two cases are considered, a low stress intensity zone (e.g. French Massif Central) and a high stress intensity zone (e.g. San Andreas Fault). It should be noted that we assume that regional stresses prevail over local stress variations, which is consistent with our homogeneity assumption. The stress profiles as a function of depth correspond to the following equations (Cornet & Burlet, 1992; Zoback, 1992):

High stress intensity:

$$\sigma_3 = 1 \times 10^6 + (15000 \times (-z))$$

$$\sigma_2 = 4 \times 10^6 + (20000 \times (-z)) \quad \text{Eq 1}$$

$$\sigma_1 = 7.5 \times 10^6 + (28667 \times (-z))$$

Low stress intensity:

$$\sigma_3 = 0.1 \times 10^6 + (13975 \times (-z))$$

$$\sigma_2 = 0.1 \times 10^6 + (26225 \times (-z)) \quad \text{Eq 2}$$

$$\sigma_1 = 0.1 \times 10^6 + (28725 \times (-z))$$

where $\sigma_1$, $\sigma_2$, $\sigma_3$, are the maximum, intermediate and minimum principal stresses, respectively. $z$ is the vertical upwards axis, and an increase in depth ($z$ <0) brings a more compressive stress (positive compression convention). We assume the constant evolution of the stress with depth. The red color code corresponds to the high stress intensity and green color code corresponds to low stress intensity. Notice that in their natural state, a strike-slip stress regime holds for both regions, i.e., $\sigma_1 = S_{Hmax}$, $\sigma_2 = S_V$, $\sigma_3 = S_{Hmin}$. In the following, we keep the realistic principal stress magnitude given in Eq 1 and Eq 2 but change in our different scenarii the axes along which they operate. This way, we are able to investigate the effect of tectonic regimes while keeping realistic stress ratios. For the understanding of the results, the color code used in Eq. 1 and Eq. 2 is the same throughout the study. In order to allow the convergence of the 3D numerical calculations with this THM coupling, the application of the stresses is applied progressively from t = 0 yrs, until t = 10 yrs. The results are shown in steady-state, at 65 kyrs for the benchmark experiment, at 990 kyrs for the model where stresses are applied. The permeability k we will consider has been empirically demonstrated to be appropriate for fractured media (Lamur et al., 2017). It is written as:

$$\log k = (1 - \omega) log k_i + \omega log k_f$$

$$k_i = 4.979 \times 10^{-11} n^{3.11} \quad \text{Eq 3}$$

$$k_f = 1.143 \times 10^{-11} n^{0.64}$$

where $\omega$ representing the degree of rock fracturing, $\omega = 1$ for fully fractured rock, and $\omega = 0$ for fully intact rock. Here we take $\omega = 0.8$ corresponding to the significant fracturing degree of the CFZ, interspersed with intact zones. $n$ the initial porosity. Here $n$ = 0.05 for intact rock, and $n$ = 0.1 for fractured rock. $k_i$ (m$^2$) the permeability of intact rock, and $k_f$ (m$^2$) the permeability of fractured rock. The stress state of a fault can be qualitatively defined in terms of slip tendency (Morris et al., 1996). In purely elastic domain and without dissipative phenomena the slip tendency is an represents indicator (high/low general trend) to assess the stress variation on a fault zone. More specifically, slip tendency indicates how critically stressed fault zones are, and how easily they can be reactivated by, e.g., stimulation methods. Consequently, some preferential flow paths may appear under the action of a given applied tectonic stress (Siler et al., 2019). The slip tendency it is defined by:

$$T_S = \frac{\tau}{\sigma'_n} \quad \text{Eq 4}$$

where $\tau$ is the shear stress and $\sigma'_n$ the effective normal stress.

$$\sigma'_n = \sigma_n - (\alpha_B \times pf) \quad \text{Eq 5}$$

where $\sigma_n$ is the total normal stress; $\alpha_B$ Biot-Willis coefficient and $pf$ fluid pressure.

# 3 Results

## 3.1 Formation of a high temperature geothermal reservoir within a vertical fault zone with no tectonic stresses, the benchmark experiment

The numerical simulation without stress application shows an upward circulation at the fault center and two downward circulations at the fault ends (Fig 1). As illustrated by colored streamlines in Figure 1, these fluid circulations transfer heat by convection. Thermally induced force is buoyancy are driving the flow. In a classical natural convection pattern, the hot fluid, less dense, goes up to the surface, cools down, and its density increases, bringing back the fluid down deeper in the fault.

Considering realistic physical conditions, no external heat source except a basal heat flux, and no mechanical stress, this free convection generates a thermal disturbance of the environment and localized the 150°C isotherm at 1.8 km depth, at the center of the fault. By comparison, in a purely diffusive setting, we would reach 150°C at 5 km depth. Fluid velocities are of the order of $1 \times 10^{-9}$ m.s$^{-1}$ at the center of the fault and $20 \times 10^{-9}$ m.s$^{-1}$ at the ends of the fault. The higher fluid velocities at the bottom center of the fault are responsible for slight increase in pressure (white lines). This trend is already observed in other numerical TH modeling (Scott et al., 2017).

The temperature gradient at the center of the model is similar to typical temperature gradient in geothermal reservoirs such as Soultz-sous-Forêts (Genter et al., 2010).

### 3.2 Application of tectonic stresses

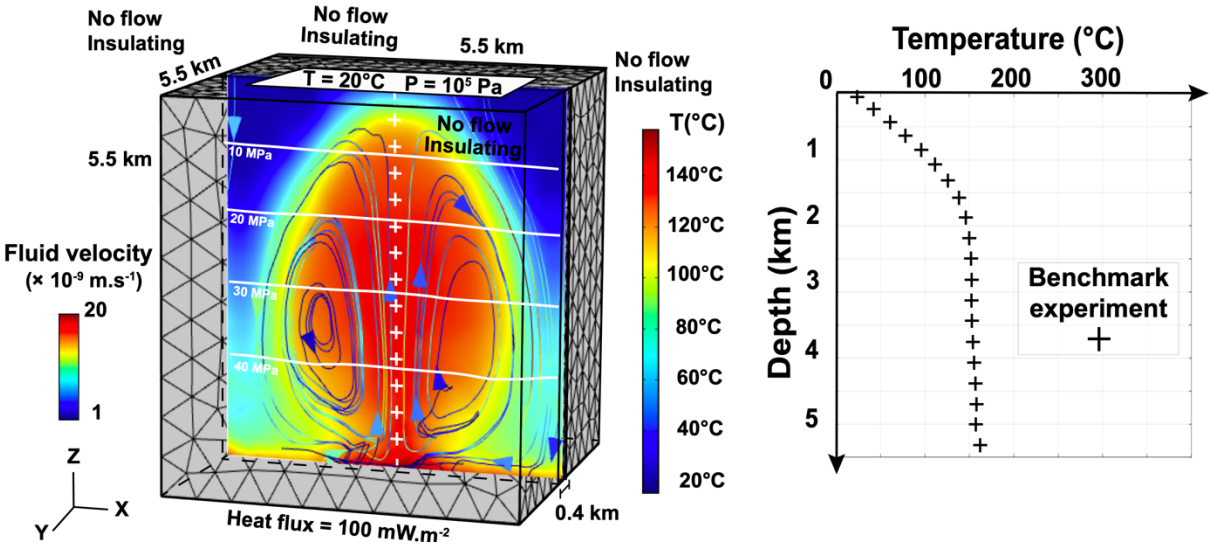


**Figure 1 :** Model setup, initial condition and results of the benchmark experiment (+) -without stress application-. Pressure (white contour), temperature (color patterns) and flow field (vectors) are displayed. The temperature profile is plotted against depth (right chart, dotted line). When free convection is established, the 150°C isotherm is located at 1.8 km depth. The benchmark experiment reaches the steady-state regime at 65 kyrs.

Figure 2 (with tectonic regimes written in red) corresponds to the high stress intensity application (see the definition of high stress intensity in the method section, Eq 1). Figure 3 (with tectonic regimes written in green) corresponds to the low stress intensity application (see the definition of low stress intensity in the method section, Eq 2). Results are shown on vertical cross sections in the fault, and on horizontal cross sections, at 2 km depth. For each tectonic regime that is considered, the results show the temperature anomalies, the fluid flow pattern and the fluid velocities. The results are different from the benchmark experiment (Fig 2 and 3).

#### 3.2.1 Different Temperature Anomalies

Regardless of the considered tectonic regime, positive and negative temperature anomalies are observed. They differ by their number, intensity and lateral extension.

**3.2.1.1** In extensional tectonic regime, two positive temperature anomalies are found (Fig 2 and 3). They are +55 °C in high stress intensity and +47 °C in low stress intensity. For both stress intensities, the second temperature anomalies are less intense, + 10°C in high stress intensity, and +7 °C in low stress intensity. For both stress intensities, a negative temperature anomaly at the center of the fault is found. This anomaly is -60°C for the high stress intensity and -57°C for the low stress intensity. For a high stress intensity, at 2 km depth, the horizontal cross-section shows a negative temperature anomaly that reaches a maximum of -30°C. This anomaly covers a large

surface area of the fault. The positive temperature anomaly of +45°C occupies the remaining space, but extends further into the basement. In the basement and up to the edge of the model, we find a positive temperature anomaly of +20°C. For a low stress intensity, at 2 km depth, two positive temperature anomalies and one negative anomaly are observed.

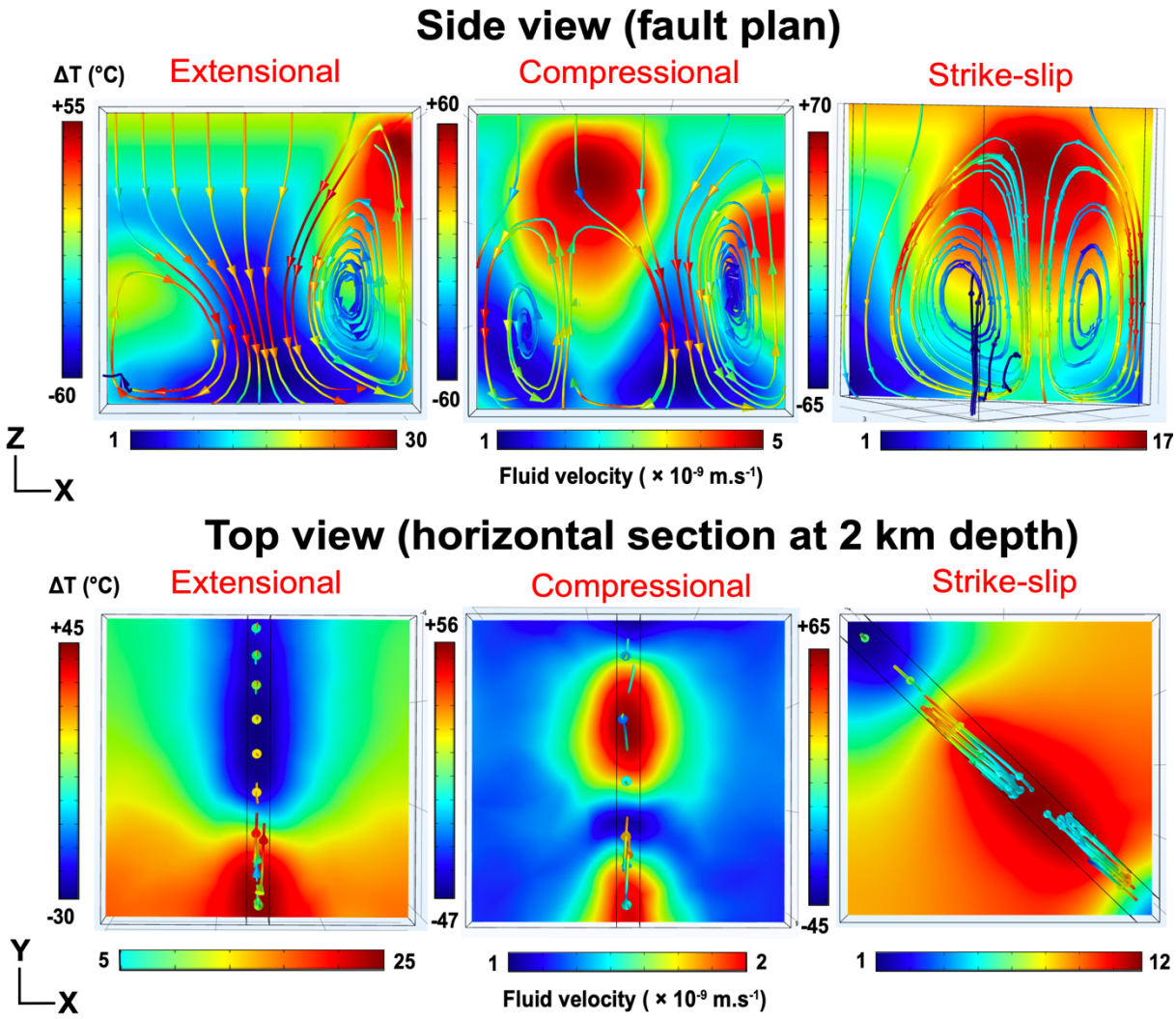


**Figure 2** : Results of numerical modeling after high stress intensity stresses application (in red, see Eq 2). The results are shown in vertical section (Side View, located in the middle of the fault) and in horizontal section, (Top view, located at 2 km depth). The scale of temperature anomalies and fluid flow velocities is different according to the tectonic regimes. For each regime, the maximum and minimum values of temperatures and fluid flow velocities are indicated. Positive temperature anomalies are colored red, negative temperature anomalies are colored blue. Fluid circulation is marked by the lines, the direction by the arrows. The color of the lines corresponds to the fluid velocity. In red the velocity is the highest, in blue the velocity is the lowest.

The first positive anomaly is +41 °C, the second has a value of +20 °C. This +20 °C anomaly spreads more widely in the system whilst the +41 °C anomaly remains localized on the fault. The

304 negative anomaly located at the center of the fault is -37 °C and extends into the basement in the
305 same way as the positive +41 °C anomaly.
306

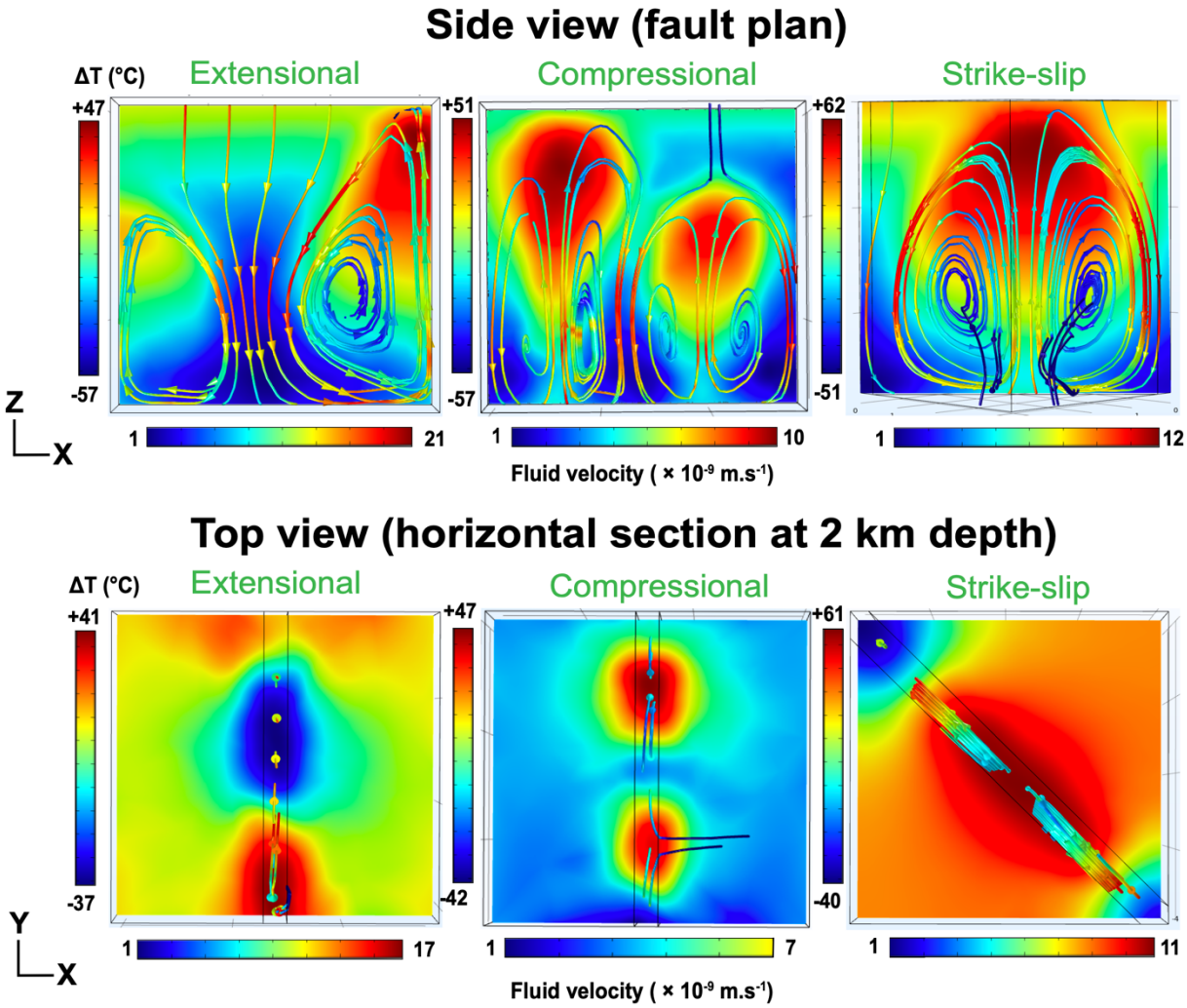


**Figure 3** : Results of numerical modeling after low stress intensity application (in green, see Eq 1). The results are shown in vertical section (Side View, located in the middle of the fault) and in horizontal section, (Top view, located at 2 km depth). The scale of temperature anomalies and fluid flow velocities is different according to the tectonic regimes. For each regime, the maximum and minimum values of temperatures and fluid flow velocities are indicated. Positive temperature anomalies are colored red, negative temperature anomalies are colored blue. Fluid circulation is marked by the lines, the direction by the arrows. The color of the lines corresponds to the fluid velocity. In red the velocity is the highest, in blue the velocity is the lowest.

307

308 **3.2.1.2** In compressional tectonic regime, independently from the stress intensity, we find two
309 positive temperature anomalies. The value of the maximum temperature anomaly in high stress
310 intensity is +60 °C and in low intensity it is +51 °C. Depending on the stress intensity, these two

maximum values are spatially slightly shifted (Fig 2 and 3). The amplitudes of the second temperature anomaly are +35°C and +40°C for low and high stress intensity, respectively. In the horizontal cross-section, the two temperature anomalies are found for each intensity. In high stress intensity the values of these two temperature anomalies are +56 °C and +47°C. In low stre stress intensity the values are +47 °C and +35 °C. The lateral extension of these temperature anomalies is limited. They are surrounded by negative temperature anomalies that locally reach -47°C in high intensity and -42°C in low intensity. At a depth of 2 km, the positive temperature anomalies are much less extended than in extensional tectonic or strike-slip regimes (see below).

**3.2.1.3** In strike-slip regimes and regardless of stress intensity applied (Fig 2 and 3), positive temperature anomaly extends widely along the length of the fault, from the surface to 4.5 km deep. The maximum positive temperature anomaly value is +70°C for the high stress intensity (Fig 2), and +62°C for the low stress intensity (Fig 3). In horizontal cross-section, these temperature anomalies spread largely beyond the fault. Temperature anomalies of + 25°C are found in the basement, suggesting that in a strike-slip system, the positive temperature anomaly, and independently from the stress intensity, represents an important volume. This heat propagation is done by thermal diffusion from the fault center, where the temperature anomaly is the most intense. Indeed, the larger the convection cell inside the fault, the wider the extent of the diffusive perturbation. At 2 km depth, the maximum value of the temperature anomaly is +65 °C for the high stress intensity, and +61 °C for the low stress intensity. Negative temperature anomalies are present and localized at the extremities of the fault. They are -45°C for the high stress intensity and -40°C for the low stress intensity.

To summarize, tectonic regimes influence the distribution and the amplitude of temperature anomalies. Positive temperature anomalies are most intense in strike-slip, then in compression and extension. The spatial extent of positive temperature anomalies is not identical for each tectonic regime. In strike-slip, these anomalies are largely extended through the basement. This lateral extension is less important in the extensive tectonic regime. Finally, in compressional regime these anomalies are localized in the near vicinity of the fault. The tectonic regimes have shown to play a key role in temperature, and this is clearly related to the different convective patterns and fluid flow velocity, as described below.

### 3.2.2 Fluid flow pattern

**3.2.2.1** In extensional tectonic regimes, the fluid flow pattern is characterized by a downward movement at the center of the fault and two upward movements at the ends of the fault (Fig 2 and 3). In high stress intensity the maximum fluid velocity is $30 \times 10^{-9}$ $m.s^{-1}$, against $21 \times 10^{-9}$ $m.s^{-1}$ in low stress intensity. The minimum fluid velocities are, for each intensity, 1 × 10-9 $m.s^{-1}$. In horizontal cross-section, at 2 km depth, upward movements are localized at positive temperature anomalies, while downward movements are localized at negative temperature anomalies. In high stress intensity, the maximum fluid velocity is $25 \times 10^{-9}$ $m.s^{-1}$, compared to 17 $\times 10^{-9}$ $m.s^{-1}$ in low stress intensity. And the minimum fluid velocity is $5 \times 10^{-9}$ $m.s^{-1}$ in high stress intensity, compared to $1 \times 10^{-9}$ $m.s^{-1}$ in low stress intensity.

**3.2.2.2** In compressional tectonic regimes, for each stress intensity, there is a slightly different convective pattern. In high stress intensity, there are two upward and two downward movements whereas in low stress intensity, there are two upward and three downward movements. The

maximum fluid velocity for high stress intensity is $5 \times 10^{-9}$ m.s$^{-1}$ and $10 \times 10^{-9}$ m.s$^{-1}$ for low stress intensity. For this tectonic regime the maximum fluid velocity is present when the lowest stress intensity is applied. In horizontal cross-section, at 2 km depth, and for high stress intensity upward movements are localized where temperature anomalies are positive whereas downward movements are localized where temperature anomalies are negative. The fluid velocity is between 1 and $2 \times 10^{-9}$ m.s$^{-1}$. In low stress intensity, the downward movements are localized at the extremities and at the center of the fault. The upward movements are localized between each downward movement. The maximum fluid velocity is $10 \times 10^{-9}$ m.s$^{-1}$ and the minimum is $1 \times 10^{-9}$ m.s$^{-1}$. At a depth of 2 km, fluid velocities vary from 1 to $2 \times 10^{-9}$ m.s$^{-1}$. Thus, fluid velocity values in compressional regime are the lowest recorded.

**3.2.2.3** In the strike-slip tectonic regime, as for the benchmark experiment, the fluid flow pattern is characterized by an upward movement at the center of the fault and two downward movements at the ends of the fault (Fig 2 and Fig 3), as observed in the benchmark experiment. The fluid velocity varies with stress intensity. In low stress intensity, the minimum fluid velocity is $1 \times 10^{-9}$ m.s$^{-1}$ and the maximum is $12 \times 10^{-9}$ m.s$^{-1}$ at the downward movements. In high stress intensity, the minimum fluid velocity is $1 \times 10^{-9}$ m.s$^{-1}$ and the maximum is $17 \times 10^{-9}$ m.s$^{-1}$.

With application of tectonic stresses; the fluid flow is different from the benchmark experiment, with consequences on temperature anomalies. In the benchmark experiment, buoyancy is the only driving force for fluid convection. Here, in presence of tectonic stresses, other forces seem to influence the fluid flow.

### 3.2.3 Lateral fluid pressure variation

After stress application, the fluid pressure is different from the benchmark experiment, where pressure is hydrostatic (Fig 4). Whatever the stress intensity applied, the experiment with compressional and strike-slip tectonic regimes show fluid pressures higher than those in the benchmark experiment, whereas, the extensional tectonic regime display fluid pressures lower than those in the benchmark experiment. The fluid pressure varies between the basement and the fault. This lateral variation differs according to the stress intensity applied.

In each of these cases, the tectonic regimes and the stress intensity generate lateral fluid pressure variation between the fault and the basement. In high stress intensity, and for the same horizontal distance, these lateral pressure differences are 1.5 MPa, 0.45 MPa, and 0.97 MPa for compressional, strike-slip, and extensional tectonic regimes, respectively. In low stress intensity the lateral pressure differences are 1.35 MPa, 0.3 MPa and 0.91 MPa for compressional, strike-slip, and extensional tectonic regimes (respectively). These lateral fluid pressure differences drive the fluids from the high-pressure zones (i.e. basement), to the low-pressure zone (i.e. fault).

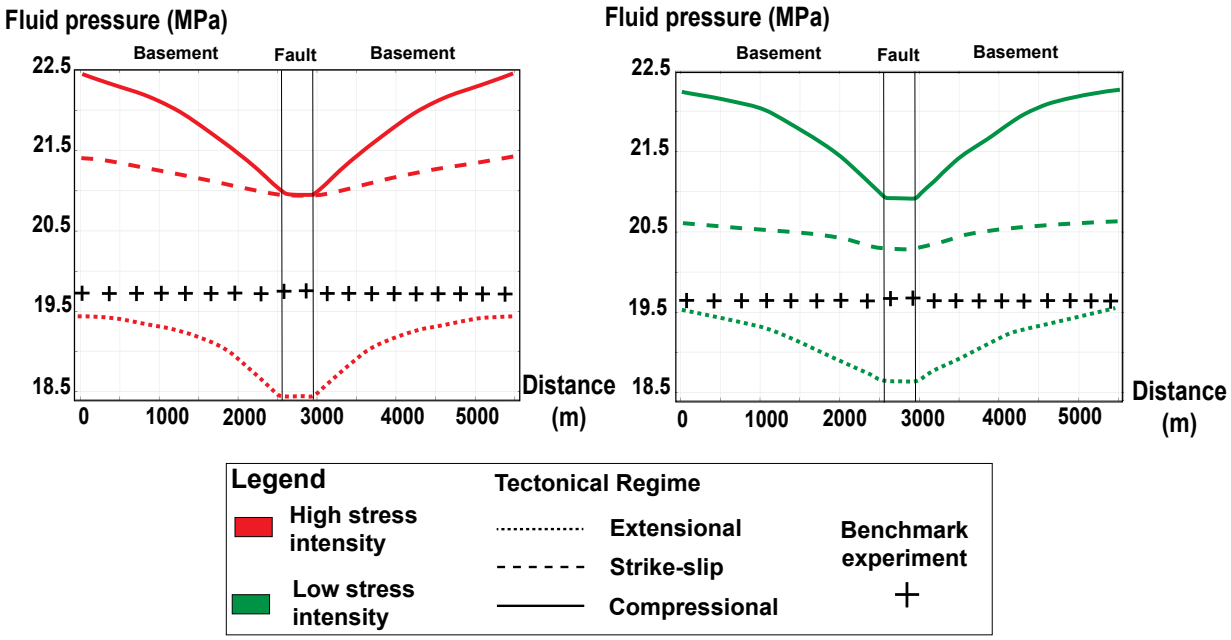


**Figure 4** : Graphs representing the lateral fluid pressure in high stress intensity application (in red), and low stress intensity application (in green). The fluid pressure of the benchmark experiment is indicated (+). With stresses application, the fluid pressure is different than the benchmark experiment. The lateral fluid pressure variation depends on the tectonic regime and stress intensity.

### 3.2.4 What effect(s) on the onset of the positive temperature ?

The regional mechanical stresses imposed a pressure distribution that will interact with buoyancy forces responsible for free convection patterns. The lateral fluid pressure differences bring the fluid from the zones of high pressure to those of low pressure. However, the time needed to set up this temperature anomaly appears to vary, as show in Figure 5.

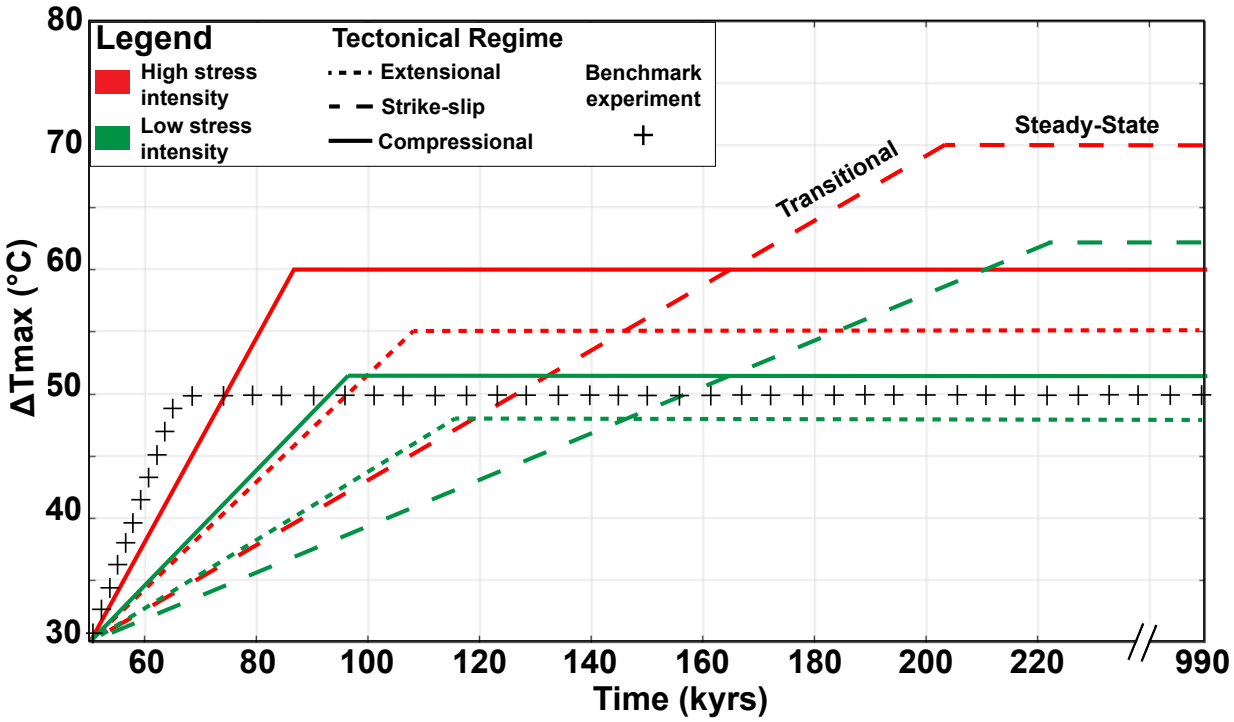


**Figure 5** : Time required to reach the steady-state temperature anomalies, depending on the tectonic regimes and the applied stress intensities. The color code and patterns are the same as those used in the previous figures.

Considering the compressional tectonic regime (solid line), the time needed to reach a steady-state regime in high stress intensity is 85 kyrs, while it is 95 kyrs in low stress intensity. This difference is observed for each regime, so that the stress intensity has a role in the setting up convection. The high stress intensity allows bringing the fluid more quickly to the zone of high permeability, and low fluid pressure. In this way, the compressional regime, which has the highest lateral fluid pressure difference, reaches the steady-state more quickly than the other tectonic regimes. The lowest lateral fluid pressure difference is recorded for the strike-slip regime. The strike-slip regime reaches the steady-state regime at 203 kyrs for high stress intensity and 223 kyrs for low stress intensity.

In a geothermal exploration context, these numerical calculations show that in a strike-slip tectonic regime the temperature anomalies should be more intense than in a compressive or extensive regime, but that the onset is the most delayed with respect to the benchmark case. The benchmark experiment reaches the steady-state regime as early as 65 kyrs, and finally the additional stress input may increase the time to reach a steady-state in situ. The differences observed on the different tectonic regimes is consistent with the differences observed on the lateral fluid pressure between the fault and the basement. However, this does not allow to explain the different fluid velocities observed (Fig 2 and 3), and the mechanical behavior of the basement-fault system after stress application.

### 3.2.5 Permeability and slip tendency variation

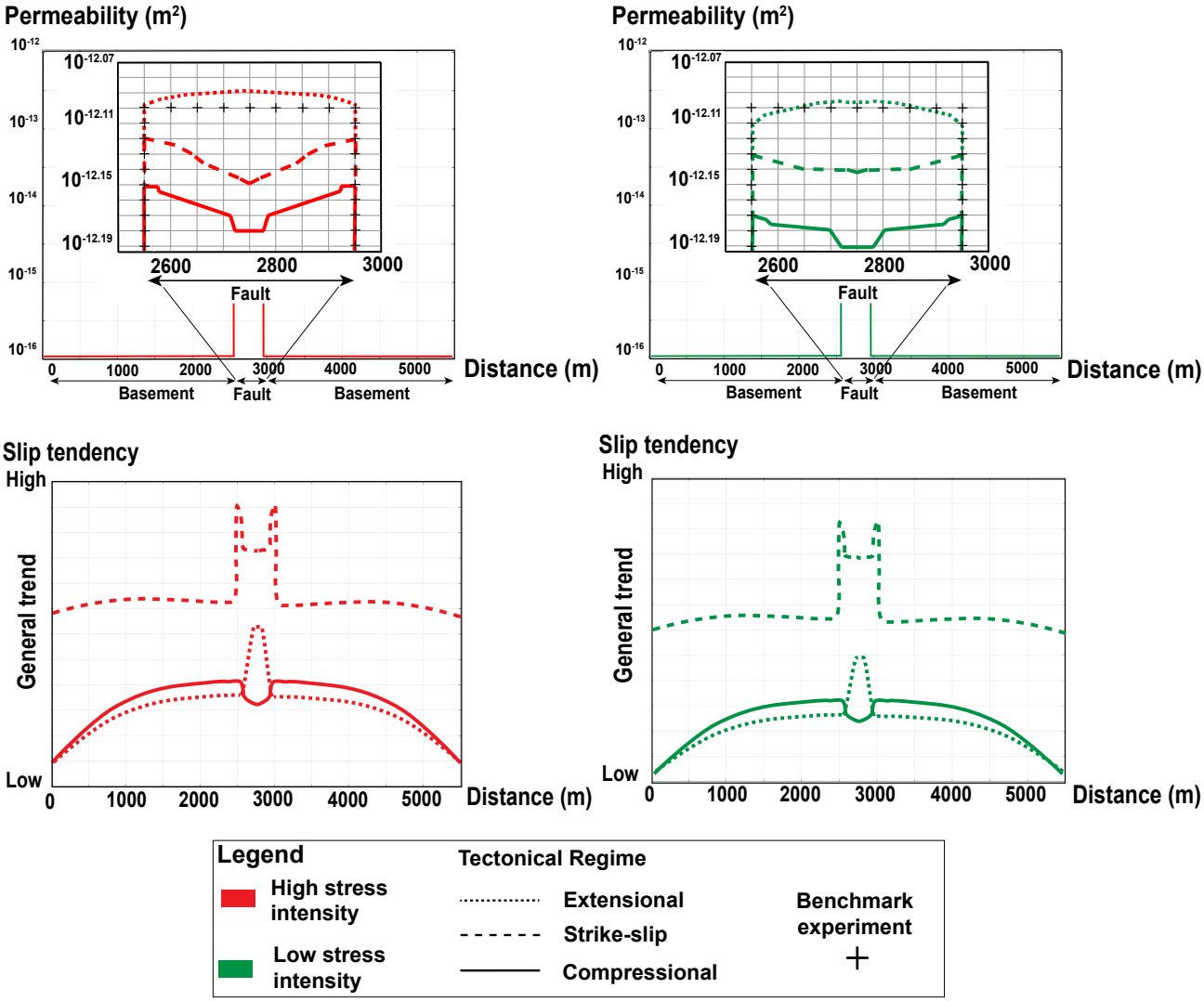


**Figure 6** : Graphs representing the permeability and the slip tendency in high stress intensity application (in red), and low stress intensity application (in green). The permeability of the benchmark experiment is indicated (+).

In the fault, very small permeability variations are observed as a function of stress intensity and tectonic regime (Fig 6). In high stress intensity, the permeability values in the center of the fault are $10^{-12.09}$, $10^{-12.15}$, 10-12.18 m2, for extensional, strike-slip and compressional tectonic regimes, respectively. In low stress intensity, the permeability values are $10^{-12.09}$, $10^{-12.14}$, $10^{-12.19}$ $m^2$, for extensional, strike-slip and compressional tectonic regimes, respectively. The effect of stress intensity on permeability remains negligible. For example, considering the compressional tectonic regime, the difference between high and low stress intensity is to 2.3 %.

To understand if these small variations in permeability between the tectonic regimes can explain the different convective patterns previously described, runs were performed considering the two

extreme values of permeability obtained: $10^{-12.09}$ and $10^{-12.19}$ $m^2$ (for more details see Appendix 2). The general thermal distribution of the system remains identical.

We note a consistency between the values of fluid velocities and permeability values. Indeed, the fluid velocities are the most important for the highest permeability, and the least important for the lowest permeability. Once the stresses are applied, the permeability are slightly different from the benchmark experiment, and control the fluid velocity.

The slip tendency is calculated and plotted for each tectonic regime and stress intensity applied (Fig 6). The global general trend is higher in high stress intensity than in low stress intensity applied. The results show a distinctive variation in the fault and in the basement for each tectonic regime. Regardless of the stress intensity applied, the slip tendency in a strike-slip tectonic regime is the highest, since it is more critically stressed. In the strike-slip regime, the slip tendency increases slightly from the edge of the basement to the level of the fault zone. At the edge of the fault, the slip tendency increases significantly. In the middle of the fault, the slip tendency slightly decreases. This evolution is the same independently from the stress intensity applied.

In compressional and extensional regimes, the trend from the edges of the basement to the fault increases similarly. This increase is slightly greater in compression than in extension. At the edge of the fault the general trend is the same. In compression the slip tendency decreases, and in extension it increases. In extension the middle of the fault is less critically stressed than in compression. Independently from the intensity of the stress this evolution is the same. Of the three tectonic regimes tested, the strike-slip regime is the most critically stressed. The general trend shows that it is at the interface between the basement and the fault that the trend is most important. This result illustrates the heterogeneity of the mechanical parameters incorporated in the numerical model, and also show that the role of the stress intensity on the range of values tested will not drastically change the mechanical response of the basement-fault system.

## 4 Discussion and Conclusion

The presence of fluids and a sufficiently high permeability are two factors to allow the development of a geothermal resource, from a natural geothermal flux. Considering a simplified geometry, but realistic physical properties (pressure and temperature dependent fluid density, temperature-dependent fluid viscosity), our 3D TH and 3D THM numerical modeling show that in a basement domain, CFZs allow hot fluids to rise to economically viable depths. The comparison of numerical models with and without tectonic stresses highlight the non-negligible role of tectonic regime on the spatial distribution of positive temperature anomalies.
Without stress application, the benchmark experiment shows that an upward movement at the center of the fault and brings a temperature of 150 °C at 1.8 km depth (Fig 1). Two downward movements are located at the ends of the fault. This convective pattern has already been observed in 2D and 3D TH numerical modeling of fault zones in the crustal domain (Wanner et al., 2019; Guillou-Frottier et al., 2020) and was called “bulb-like” convective pattern. This particular shape is favored because hot fluids have less resistance when flowing upwards (viscosity is smaller at high temperature) and can localize temperature anomalies also in the

493 basement. With a flat topography and without metamorphic devolatilization and/or magmatic
494 fluid production that might change fluid pressure (Nur and Walder, 1990), fluid circulation is
495 only driven by the buoyancy force. With tectonic regimes application, we have seen that other
496 forces are added and modify the fluid circulation.
497
498 Considering the experiments where tectonic regimes are accounted for, the obtained results are
499 different from the benchmark experiment (Fig 2 and Fig 3). This highlights the key role of the
500 relationship between tectonic settings and fluid flow. In our results, the stress intensity parameter
501 does not change the general dynamics of convective patterns between two identical regimes.
502 Considering a sensitivity study on a large Pontgibaud Crustal Fault Zone (French Massif
503 Central), where the stresses boundary magnitudes are tested while holding their directions, a shift
504 from one convective pattern to another would occur for a variation of approximately 40 MPa in
505 the maximum horizontal stress magnitude (Duwiquet et al., 2021). For this last example and in
506 the light of the observations made in this study, it could be possible that another force than the
507 buoyancy, influences fluid circulation. In this study the stress intensity applied is not a factor
508 influencing the convection pattern. However, the stress intensity has a role in the time to reach
509 the steady-state. Indeed, the steady-state is reached faster when the most intense stresses are
510 applied (Fig 5), and this was not explored in the Duwiquet et al. (2021) study. Moreover, the role
511 of tectonics on the direction of fluid flow has been highlighted. Considering a numerical
512 approach, studies have shown that in compression, upward fluid movements are favored (Upton,
513 1998), whereas in extension, downward fluid movements are favored (Cui et al., 2012). Here we
514 could see that the different tectonic regimes will have a role in the onset of convection. This
515 element also explains the final results observed.
516
517 These numerical models show that the tested tectonic regimes have an influence on fluid
518 pressure variation. The poroelastic assumption describes the interaction of fluids and
519 deformation in porous media. Compressional, extensional, and strike-slip tectonic regimes
520 induce variable fluid pressures for each case. The incorporation of heterogeneous mechanical
521 parameters between the fault and the basement (see Table 1) leads to a different mechanical
522 response and thus to a heterogeneous variation of the fluid pressure between the fault and the
523 basement (see Fig 4). This lateral fluid pressure difference drives the fluids from the high-
524 pressure zones to the low-pressure zones. This effect is facilitated by higher permeability values
525 in the fault than in the basement.
526
527 This force, which drives fluids from high pressure zones to low pressure zones is similar to the
528 effects of topography on fluid flow (Forster and Smith, 1989; López and Smith, 1995). This
529 poroelasticity driven force will therefore influence the initial fluid motions (downward and
530 upward movement) and thus the time required for the steady-state temperature anomaly to
531 develop. Considering a TH coupling, the fluid circulation in the benchmark experiment is driven
532 by free convection. Considering three different tectonic regimes with the same TH coupling, the
533 fluid circulation is the result of an interplay between forced and free convection. These changes
534 are not related to boundary conditions, but to the tectonic regimes themselves. Forced convection
535 is referred to as stress induced convection.
536
537 After stress applications, the permeability values obtained are consistent with fractured and
538 altered granitic environment (Sardini et al., 1997; Duwiquet et al., 2019; 2021; Gomila et al.,

2021). This should be sufficient to allow fluids to flow by buoyancy forces and transfer heat by free convection. However, between tectonic regimes, the difference in permeability cannot explain convective pattern variability results. Nevertheless, these small permeability variations influence the velocities of fluid flow. The fluid velocity decreases with a permeability decrease (see Fig 2, 3, and 6). Actually, the positive temperature anomalies in the compression and extensional regime model remain centered on the fault compared to the extensional and strike-slip tectonic regimes. Therefore, other processes must limit the development of temperature anomalies in compressional regime. By concentrating the flow of fluids on limited spaces, the poroelasticity driven force could have the effect of spatially concentrating temperature anomalies when the difference between the fluid pressure of the basement and the fault is large.

For geothermal exploration, slip tendency analyses can be used to target favorable zones for natural fluid flow and future enhancement by fault reactivation (Barton et al., 1995; Morris et al., 1996; Ito and Zoback, 2000). Our results show that the strike-slip regime would be the most favorable to allow fluid flow. The occurrence of geothermal reservoirs in such contexts is already known, Alpine Fault, New Zealand (Boulton et al., 2012), the Geysers (Altmann et al., 2013). In the light of our results, an exploratory phase on the geothermal potential of fault zones could further consider strike-slip faulted as interesting targets for geothermal power system.

If slip tendency can be used as a potential qualitative indicator in purely elastic models, a more accurate interpretation would require incorporating dissipative mechanical behaviors such as, e.g., Mohr-Coulomb elasto-plastic law, which would allow to quantify the variation in slip tendency. By considering irreversible mechanical processes, including dilation (opening under shearing) and fracturing (increase of pore space/fractures), the best favorability of strike-slip regime towards convection is expected to be emphasized.

We used an idealized geometry with single, vertical fault zone. The linear stress boundary conditions hence give rather homogeneous stress ratios and states along the fault. In natural systems, the network of variously oriented and dipping fault zones brings heterogeneous stress states, even along each fault zone taken separately. Still, and recalling that the aim of our study is to better understand the setup conditions of convection cells, the results already allow us to highlight the complex impact of mechanics over convection patterns. Among others, our conclusions tend to show that within a complex fault zone network, fault zones undergoing strike-slip conditions might be the ones to be preferably explored.

These fundamental results are generally applicable in nature to any facture rock that may contain fluids, gas or oil in its pores, in basement geological context. However, our results do not take into account fundamental aspects such as the consideration of more complex rheology, to start with plastic phenomena. The effects of fault intersections, precipitation and dissolution of mineral phases, and fluid composition were also not taken into account. The dependence of permeability on all of these phenomena should probably generate permeability anisotropy. The development of this anisotropy can cause a change in the intrinsic properties of the geothermal reservoir and induce a change in the heat transfer mode (Sun et al., 2017). In cases where fluid flow is important (i.e. areas of high permeability) the permeability can take a particular geometry minimizing the resistance to flow and then optimizing fluid flow (Bejan and Lorente, 2011).

584 Fluid salinity could also play an important role, but effects would be marked above 400°C
585 (Driesner, 2007), which is beyond our modeled temperatures.
586
587 Geothermal energy can become a major asset for the transition to low-carbon energy sources. Its
588 development requires, prior to exploration, comprehensive understanding of limiting and
589 enabling factors controlling fluid flow and the location of temperature anomalies (Jolie et al.,
590 2021). Our numerical results show that the poroelasticity driven force provoked by the tectonic
591 regimes causes lateral fluid pressure variation, allowing for the more or less rapid development
592 of the temperature anomaly, by mixed, free and forced convection. For example, strike-slip
593 tectonic regimes would have the largest temperature anomalies, but would take the longest time
594 to set up.
595
596 Overall, this work suggests that anomalously permeable zone, like CFZ, with no external heat
597 source, have significant energy potential. The exploration of the vertical Crustal Fault Zones in
598 strike-slip stress regime, could accelerate the transition to low-carbon, renewable and climate-
599 neutral energy. Studies have already shown that major strike-slip fault zones localize porosity
600 and permeability even beyond the BDT (Faulkner et al., 2010; Cao and Neubauer, 2016). Our
601 study confirms that this tectonic regime seems to favor higher thermal anomalies than
602 compressional tectonics.
603
604 The complex nature of the processes occurring during the development of a geothermal resource
605 within a CFZ makes it an environment that requires a state-of-the-art numerical analysis of the
606 process that can control the fluid circulation. Such fully coupled analysis will help exploration
607 phases and ultimately promote the development of this renewable energy, not only in
608 anomalously hot areas, but in anomalously permeable areas, and thus promote the development
609 of this climate-neutral energy.

610 **References**

611
612 Altmann, J. B., Heidbach, O., & Gritto, R. (2013). Relative importance of processes leading to
613 stress changes in the Geysers geothermal area. *In Proceedings of thirty-eighth workshop on*
614 *geothermal reservoir engineering*.
615
616 Anderson, E. M. (1905). The dynamics of faulting. *Transactions of the Edinburgh Geological*
617 *Society*. 8(3), 387- 402. https://doi.org/10.1144/transed.8.3.387.
618
619 Barton, C. A., Zoback, M. D., & Moos, D. (1995). Fluid flow along potentially active faults in
620 crystalline rock. *Geology*. 23(8), 683-686. https://doi.org/10.1130/0091-
621 7613(1995)023<0683:FFAPAF>2.3.CO;2
622
623 Bejan, A., & Lorente, S. (2011) The constructal law and the evolution of design in
624 nature. *Physics of life Reviews*, 8(3), 209-240. https://doi.org/10.1016/j.plrev.2011.05.010.
625
626 Bethke, C. M. (1985). A numerical model of compaction-driven groundwater flow and heat
627 transfer and its application to the paleohydrology of intracratonic sedimentary basins. *Journal of*

628 *Geophysical Research: Solid Earth*. 90(B8), 6817-6828.
629 https://doi.org/10.1029/JB090iB08p06817
630
631 Ben-Zion, Y., & Rovelli, A. Properties and Processes of Crustal Fault Zones: Volume I. *Pure*
632 *and Applied Geophysics*. 171(11), 2863-2865 (2014).
633 https://doi.org/10.1007/s00024-014-0943-3
634
635 Cappa, F., & Rutqvist, J. (2011). Impact of CO2 geological sequestration on the nucleation of
636 earthquakes. *Geophysical Research Letters*. 38(17). https://doi.org/10.1029/2011GL048487.
637
638 Cao, S., & Neubauer, F. (2016). Deep crustal expressions of exhumed strike-slip fault systems:
639 Shear zone initiation on rheological boundaries. *Earth-Science Reviews*. 162, 155-176.
640 https://doi.org/10.1016/j.earscirev.2016.09.010
641
642 Cornet, F. H., & Burlet, D. (1992). Stress field determinations in France by hydraulic tests in
643 boreholes. *Journal of Geophysical Research: Solid Earth*. 97(B8), 11829-11849.
644 https://doi.org/10.1029/90JB02638.
645
646 Cox, S. F. (2005). Coupling between deformation, fluid pressures, and fluid flow in ore-
647 producing hydrothermal systems at depth in the crust. *Economic Geology*. 100, 39-75.
648
649 Cox, S. F. (1999). Deformational controls on the dynamics of fluid flow in mesothermal gold
650 systems. *Geological Society, London, Special Publications*. 155(1), 123-140.
651 https://doi.org/10.1144/GSL.SP.1999.155.01.10
652
653 Cui, T., Yang, J., & Samson, I. M. (2012).Tectonic deformation and fluid flow: implications for
654 the formation of unconformity-related uranium deposits. *Economic Geology*. 107(1), 147-163.
655 https://doi.org/10.2113/econgeo.107.1.147.
656
657 Deichmann, N., and Giardini, D. (2009). Earthquakes induced by the stimulation of an enhanced
658 geothermal system below Basel (Switzerland). *Seismological Research Letters*. 80(5), 784-798.
659 https://doi.org/10.1785/gssrl.80.5.784.
660
661 Driesner, T. (2007) The system H2O–NaCl. Part II: Correlations for molar volume, enthalpy, and
662 isobaric heat capacity from 0 to 1000 C, 1 to 5000 bar, and 0 to 1 XNaCl. *Geochimica et*
663 *Cosmochimica Acta*. 71(20), 4902-4919. https://doi.org/10.1016/j.gca.2007.05.026.
664
665 Duwiquet, H., Arbaret, L., Guillou-Frottier, L., Heap, M. J., Bellanger, M. (2019). On the
666 geothermal potential of crustal fault zones: a case study from the Pontgibaud area (French Massif
667 Central, France). *Geothermal Energy*. 7(1), 1-29. https://doi.org/10.1186/s40517-019-0150-7.
668
669 Duwiquet, H., Guillou-Frottier, L., Arbaret, L., Bellanger, M., Guillon, T., Heap, M. J. (2021)
670 Crustal Fault Zones (CFZ) as Geothermal Power Systems: A Preliminary 3D THM Model
671 Constrained by a Multidisciplinary Approach. *Geofluids*. 2021.
672 https://doi.org/10.1155/2021/8855632
673

Duwiquet, H., Guillou-Frottier, L., Arbaret, L., Bellanger, M., Guillon, T., Heap, M. J Crustal Fault Zones (CFZ) as Geothermal Power Systems: 3D Variation of Permeability and Related Processes. In Stanford Geothermal Workshop. (2021, February)

Eldursi, K., Chi, G., Bethune, K., Li, Z., Ledru, P., & Quirt, D. (2020). New insights from 2-and 3-D numerical modelling on fluid flow mechanisms and geological factors responsible for the formation of the world-class Cigar Lake uranium deposit, eastern Athabasca Basin, Canada. *Mineralium Deposita*. 1-24. https://doi.org/10.1007/s00126-020-00979-5.

Evans, K. F. et al. (2005). Microseismicity and permeability enhancement of hydrogeologic structures during massive fluid injections into granite at 3 km depth at the Soultz HDR site. *Geophysical Journal International*. 160(1), 388-412. https://doi.org/10.1111/j.1365-246X.2004.02474.x.

Famin, V., Philippot, P., Jolivet, L., & Agard, P. (2004). Evolution of hydrothermal regime along a crustal shear zone, Tinos Island, Greece. *Tectonics*. 23(5). https://doi.org/10.1029/2003TC001509.

Faulkner, D. R., Lewis, A. C., & Rutter, E. H. (2003). On the internal structure and mechanics of large strike-slip fault zones: field observations of the Carboneras fault in southeastern Spain. *Tectonophysics*, 367(3-4), 235-251. https://doi.org/10.1016/S0040-1951(03)00134-3

Faulkner, D. R., Jackson, C. A. L., Lunn, R. J., Schlische, R. W., Shipton, Z. K., Wibberley, C. A. J., & Withjack, M. O. (2010). A review of recent developments concerning the structure, mechanics and fluid flow properties of fault zones. *Journal of Structural Geology*. **32(11)**, 1557-1575. https://doi.org/10.1016/j.jsg.2010.06.009

Forster, C., & Smith, L. (1989). The influence of groundwater flow on thermal regimes in mountainous terrain: A model study. *Journal of Geophysical Research: Solid Earth*. 94(B7), 9439-9451. https://doi.org/10.1029/JB094iB07p09439.

Gomila, R., Arancibia, G., Nehler, M., Bracke, R., Morata, D., & Cembrano, J. (2021). Quantitative anisotropies of palaeopermeability in a strike-slip fault damage zone: Insights from micro-CT analysis and numerical simulations. *Tectonophysics*, 228873. https://doi.org/10.1016/j.tecto.2021.228873

Genter, A., Evans, K., Cuenot, N., Fritsch, D., Sanjuan, B. (2010) Contribution of the exploration of deep crystalline fractured reservoir of Soultz to the knowledge of enhanced geothermal systems (EGS). *Comptes Rendus Geoscience*. 342(7-8), 502-516. https://doi.org/10.1016/j.crte.2010.01.006

Gleeson, T., & Ingebritsen, S. (Eds.). Crustal permeability. John Wiley & Sons. (2016).

718 Glover, P. W. J., Matsuki, K., Hikima, R., & Hayashi, K. (1998). Fluid flow in synthetic rough
719 fractures and application to the Hachimantai geothermal hot dry rock test site. *Journal of*
720 *Geophysical Research: Solid Earth*. 103(B5), 9621-9635. https://doi.org/10.1029/97JB01613
721
722 Grawinkel, A., & Stöckhert, B. (1997). Hydrostatic pore fluid pressure to 9 km depth-Fluid
723 inclusion evidence from the KTB deep drill hole. *Geophysical Research Letters*. 24(24), 3273-
724 3276. https://doi.org/10.1029/97GL03309
725
726 Guillou-Frottier, L., Carrė, C., Bourgine, B., Bouchot, V., & Genter, A. (2013). Structure of
727 hydrothermal convection in the Upper Rhine Graben as inferred from corrected temperature data
728 and basin-scale numerical models. *Journal of Volcanology and Geothermal Research*. 256, 29-
729 49. https://doi.org/10.1016/j.jvolgeores.2013.02.008
730
731 Guillou-Frottier. L., Duwiquet, H., Launay, G., Taillefer, A., Roche, V., & Link, G. (2020). On
732 the morphology and amplitude of 2D and 3D thermal anomalies induced by buoyancy-driven
733 flow within and around fault zones. *Solid Earth*. 11(4), 1571-1595. https://doi.org/10.5194/se-11-
734 1571-2020.
735
736 Heap, M. J., et al. (2020). Towards more realistic values of elastic moduli for volcano
737 modelling. *Journal of Volcanology and Geothermal Research*. 390, 10668.
738 https://doi.org/10.1016/j.jvolgeores.2019.106684.
739
740 Horton, C. W., & Rogers Jr, F. T. (1945). Convection currents in a porous medium. *Journal of*
741 *Applied Physics*. 16(6), 367-370. https://doi.org/10.1063/1.1707601.
742
743 Horne, R. N. (1979). Three-dimensional natural convection in a confined porous medium heated
744 from below. *Journal of Fluid Mechanics*. 92(4), 751-766.
745
746 Ito, T., & Zoback, M. D. (2000). Fracture permeability and in situ stress to 7 km depth in the
747 KTB scientific drillhole. *Geophysical Research Letters*. 27(7), 1045-1048.
748 https://doi.org/10.1029/1999GL011068
749
750 Katto, Y., & Masuoka, T. (1967). Criterion for the onset of convective flow in a fluid in a porous
751 medium. *International Journal of Heat and Mass Transfer*. 10(3), 297-309.
752 https://doi.org/10.1016/0017-9310(67)90147-0.
753
754 Kozlovsky, Y. (1984). The World's Deepest Well. Scientific American, 251(6), 98-105. from
755 http://www.jstor.org/stable/24969503
756
757 Kwiatek, G., Bohnhoff, M., Dresen, G., Schulze, A., Schulte, T., Zimmermann, G., & Huenges,
758 E. (2010). Microseismicity induced during fluid-injection: A case study from the geothermal site
759 at Groß Schönebeck, North German Basin. Acta Geophysica. 58(6), 995-1020.
760 https://doi.org/10.2478/s11600-010-0032-7
761

762 Lamur, A., Kendrick, J. E., Eggertsson, G. H., Wall, R. J., Ashworth, J. D., & Lavallée, Y.
763 (2017). The permeability of fractured rocks in pressurised volcanic and geothermal
764 systems. *Scientific reports*. 7(1), 1-9. https://doi.org/10.1038/s41598-017-05460-4.
765
766 Ledingham, P., Cotton, L., & Law, R. (2019). The united downs deep geothermal power
767 project. *Proc. 44th Work. Geotherm. Reserv. Eng*, 1-11.
768
769 López, D. L., & Smith, L. (1995).Fluid flow in fault zones: analysis of the interplay of
770 convective circulation and topographically driven groundwater flow. *Water resources*
771 *research*. 31(6), 1489-1503. https://doi.org/10.1029/95WR00422.
772
773 Liang, X., Xu, T., Feng, B., & Jiang, Z. (2018). Optimization of heat extraction strategies in
774 fault-controlled hydro-geothermal reservoirs. *Energy*. 164, 853-870.
775 https://doi.org/10.1016/j.renene.2019.02.070
776
777 Magri, F., Cacace, M., Fischer, T., Kolditz, O., Wang, W., & Watanabe, N. (2017).Thermal
778 convection of viscous fluids in a faulted system: 3D benchmark for numerical codes. Energy
779 Procedia. 125, 310-317. https://doi.org/10.1016/j.egypro.2017.08.204
780
781 McLellan, J. G., Oliver, N. H. S., & Schaubs, P. M. (2004). Fluid flow in extensional
782 environments; numerical modelling with an application to Hamersley iron ores. *Journal of*
783 *Structural Geology*. 26(6-7), 1157-1171. https://doi.org/10.1016/j.jsg.2003.11.015
784
785 Morris, A., Ferrill, D. A., Henderson, D. B. (1996). Slip-tendency analysis and fault
786 reactivation. *Geology*. 24(3), 275-278. https://doi.org/10.1130/0091-
787 7613(1996)024<0275:STAAFR>2.3.CO;2
788
789 O'Sullivan, M. J., Pruess, K., & Lippmann, M. J. (2001) State of the art of geothermal reservoir
790 simulation. *Geothermics*. 30(4), 395-429. https://doi.org/10.1016/S0375-6505(01)00005-0.
791
792 Ord, A., & Oliver, N. H. S. (1997) Mechanical controls on fluid flow during regional
793 metamorphism: some numerical models. *Journal of Metamorphic Geology*. 15(3), 345-359.
794 https://doi.org/10.1111/j.1525-1314.1997.00030.x
795
796 Parisio, F., Vilarrasa, V., Wang, W., Kolditz, O., Nagel, T. (2019) The risks of long-term re-
797 injection in supercritical geothermal systems. *Nature communications*. 10(1), 1-11.
798 https://doi.org/10.1038/s41467-019-12146-0
799
800 Paulillo, A., Cotton, L., Law, R., Striolo, A., & Lettieri, P. (2020). Geothermal energy in the UK:
801 The life-cycle environmental impacts of electricity production from the United Downs Deep
802 Geothermal Power project. *Journal of Cleaner Production*, 249, 119410.
803
804 Phillips, W. J. (1972). Hydraulic fracturing and mineralization. *Journal of the Geological*
805 *Society*. 128(4), 337-359.
806

807 Rowland, J. V., & Sibson, R. H. (2004). Structural controls on hydrothermal flow in a segmented
808 rift system, Taupo Volcanic Zone, New Zealand. *Geofluids*. 4(4), 259-283.
809 https://doi.org/10.1111/j.1468-8123.2004.00091.x
810
811 Saevarsdottir, G., Tao, P. C., Stefansson, H., & Harvey, W. (2014). Potential use of geothermal
812 energy sources for the production of lithium-ion batteries. *Renewable energy*. 61, 17-22.
813 https://doi.org/10.1016/j.renene.2012.04.028
814
815 Sardini, P., Ledésert, B., & Touchard, G. (1997). Quantification of microscopic porous networks
816 by image analysis and measurements of permeability in the Soultz-sous-Forêts granite (Alsace,
817 France). *In Fluid flow and Transport in rocks*. 171-189. https://doi.org/10.1007/978-94-009-
818 1533-6_10
819
820 Scott, S., Driesner, T., & Weis, P. (2017). Boiling and condensation of saline geothermal fluids
821 above magmatic intrusions. *Geophysical Research Letters*. 44(4), 1696-1705.
822 https://doi.org/10.1002/2016GL071891.
823
824 Sibson, R. H. (1987). Earthquake rupturing as a mineralizing agent in hydrothermal
825 systems. *Geology*. 15(8), 701-704. https://doi.org/10.1130/0091-
826 7613(1987)15<701:ERAAMA>2.0.CO;2
827
828 Siebenaller, L. et al. (2013). Fluid record of rock exhumation across the brittle–ductile transition
829 during formation of a Metamorphic Core Complex (Naxos Island, Cyclades, Greece). *Journal of*
830 *Metamorphic Geology*. 31(3), 313-338. https://doi.org/10.1111/jmg.12023
831
832 Siler, D. L. Faulds, J. E., Hinz, N. H., Dering, G. M., Edwards, J. H., & Mayhew, B. (2019).
833 Three-dimensional geologic mapping to assess geothermal potential: examples from Nevada and
834 Oregon. *Geothermal Energy***.** 7(1), 1-32. https://doi.org/10.1186/s40517-018-0117-0.
835
836 Sun, Z. X. et al. (2017). Numerical simulation of the heat extraction in EGS with thermal-
837 hydraulic-mechanical coupling method based on discrete fractures model. *Energy*. 120, 20-33.
838 https://doi.org/10.1016/j.energy.2016.10.046.
839
840 Violay, M., Heap, M. J., Acosta, M., & Madonna, C. Porosity evolution at the brittle-ductile
841 transition in the continental crust: Implications for deep hydro-geothermal circulation. *Scientific*
842 *reports*. **7(1)**, 1-10 (2017). https://doi.org/10.1038/s41598-017-08108-5.
843
844 Wanner, C., Diamond, L. W., & Alt-Epping, P. (2019). Quantification of 3-D thermal anomalies
845 from surface observations of an orogenic geothermal system (Grimsel Pass, Swiss Alps). *Journal*
846 *of Geophysical Research: Solid Earth*. 124(11), 10839-10854.
847 https://doi.org/10.1029/2019JB018335
848
849 Watanabe, N., Egawa, M., Sakaguchi, K., Ishibashi, T., & Tsuchiya, N. (2017). Hydraulic
850 fracturing and permeability enhancement in granite from subcritical/brittle to
851 supercritical/ductile conditions. *Geophysical Research Letters*. 44(11), 5468-5475.
852 https://doi.org/10.1002/2017GL073898.

Watanabe, N., Abe, H., Okamoto, A., Nakamura, K., & Komai, T. (2021). Formation of amorphous silica nanoparticles and its impact on permeability of fractured granite in superhot geothermal environments. *Scientific reports*. 11(1), 1-11. https://doi.org/10.1038/s41598-021-84744-2

Wilson, M. P., Foulger, G. R., Gluyas, J. G., Davies, R. J., & Julian, B. R. (2017). HiQuake: The human-induced earthquake database. Seismological Research Letters, 88(6), 1560-1565. Data set https://doi.org/10.1785/0220170112 (2017). https://inducedearthquakes.org

Zareidarmiyan, A., Parisio, F., Makhnenko, R. Y., Salarirad, H., & Vilarrasa, V. (2021) How equivalent are equivalent porous media? *Geophysical Research Letters*, e2020GL089163. https://doi.org/10.1029/2020GL089163.

Zoback et al. (2003). Determination of stress orientation and magnitude in deep wells. *International Journal of Rock Mechanics and Mining Sciences*. 40(7-8), 1049-1076. https://doi.org/10.1016/j.ijrmms.2003.07.001.

Zoback, M. L. (1992). Stress field constraints on intraplate seismicity in eastern North America. *Journal of Geophysical Research: Solid Earth*. 97(B8), 11761-11782. https://doi.org/10.1029/92JB00221.

## Appendices

## Appendix 1

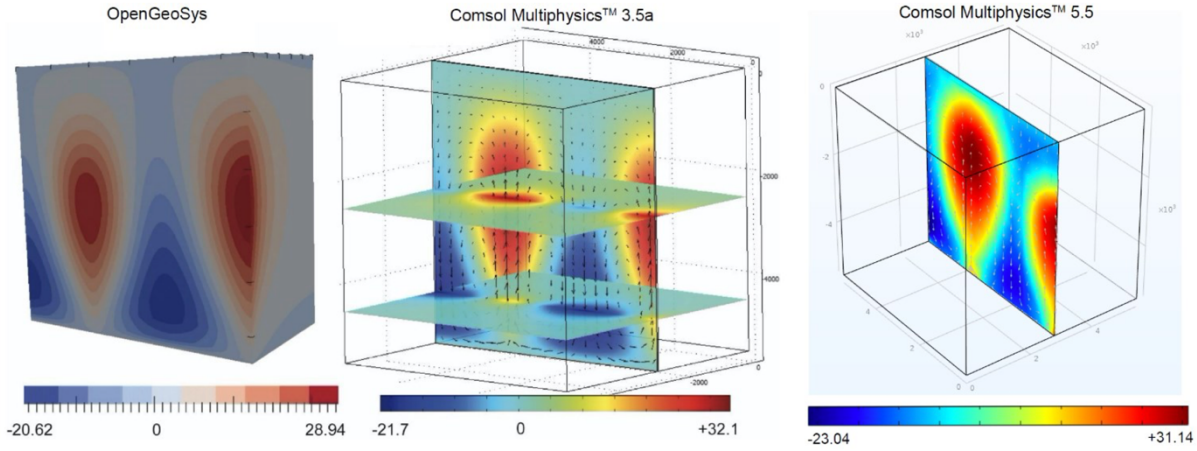


**Appendix 1** : Benchmarking of our numerical experiment with the OpenGeoSys Code (Magri et al. 2017) and Comsol Multiphysics™ V3.5a (Guillou-Frottier et al. 2020) (From Duwiquet et al. 2021).

879 The calibration of our numerical experiments was performed based on results from Comsol
880 Multiphysics$^{TM}$ version 3.5 (Guillou-Frottier et al., 2020) as well as the OpenGeoSys numerical
881 code (Magri et al., 2017). These models consider a 40 m wide vertical fault in an impermeable
882 box (a 5.5*5.5*5.5 km side cube). The fluid properties are identical for all three results with a
883 linear dependence of temperature with water density, and an exponential decrease of viscosity
884 with temperature. This result is shown for a time $t_0 + 10^{13}$ s. The imposed permeability value is 5
885 $\times 10^{-15}$ $m^2$. The fluid flow velocity is $2.03 \times 10^{-9}$ $m.s^{-1}$. The fluid flow velocity is slightly higher
886 than that described by Guillou-Frottier et al. (2020), who record a velocity of $1.4 \times 10^{-9}$ $m.s^{-1}$.
887 The convective patterns are similar. Fluid velocity accelerates along the permeable fault and
888 exhibits upward movement due to the thermal gradient and buoyancy forces related to lower
889 water density at depth. The thermal perturbations are also within the orders of magnitude of
890 previous studies with -22.04°C and +31.14 °C.

891 The numerical experiments of Magri et al. (2017) and Guillou-Frottier et al. (2020) used Darcy's
892 law in conjunction with the equations of heat. The numerical experiments of this study couple
893 the equations of heat and mass transfer with the modulus of poroelasticity. The poroelasticity
894 interface of Comsol Multiphysics$^{TM}$ combines Darcy's law with the linear elastic behavior of
895 porous media (details can be found in Duwiquet et al., 2021). Poroelastic coupling allows
896 boundary stresses to be imposed, which can be recorded as fluid pressure. In Appendix 1 (right),
897 no stress or other mechanical conditions are applied. Consequently, this experiment corresponds
898 to an identical coupling as in the previous studies (App 1, left and middle cases).

899

## Appendix 2

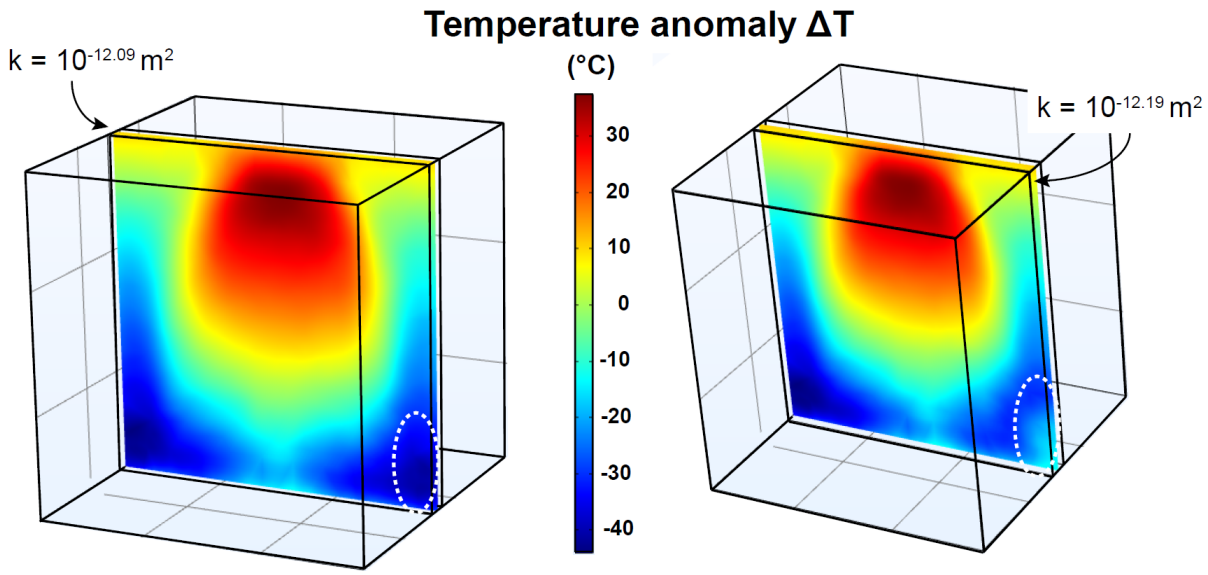


**Appendix 2** : Comparison of the numerical results with a TH coupling considering as the only difference, a permeability variation of the order of $10^{-0.10}$ $m^2$. The results of the numerical calculations show no difference in the calculated values (see color bar). In cross-section, parallel to the fault, the difference is only at the bottom right of the numerical model.

In order to understand if the permeability variations obtained after the stress application can explain the differences observed between the tectonic regimes, two numerical calculations with only a TH coupling have been performed. The parameters and their geometries are identical, the only difference is the permeability variation. On the left, a permeability of $10^{-12.09}$ $m^2$ is imposed on the fault, on the right a permeability of $10^{-12.19}$ $m^2$ is imposed on the fault. The results are similar. The only difference is located at the bottom right of the fault. On the left, the anomaly is -40°C, on the right it is -12°C. This localized difference does not seem to influence the thermal distribution of the overall system.